Int J Fract (2020) 225:47–67
https://doi.org/10.1007/s10704-020-00463-1

ORIGINAL PAPER

A void descriptor function to uniquely characterize pore networks and predict ductile-metal failure properties

John M. Erickson · Aowabin Rahman · Ashley D. Spear

Received: 10 February 2020 / Accepted: 10 June 2020 / Published online: 24 June 2020

Abstract Porosity, a commonly occurring void defect in casting and additive manufacturing, is known to affect the mechanical response of metals, making it difficult or impossible to predict response variability. We introduce a new method of uniquely characterizing pore networks using a void descriptor function (VDF), which can be used to predict ductile-metal failure properties, namely, toughness modulus, ultimate strength, elongation, and fracture location. The VDF quantifies the inter-relationships of pores by accounting for pore location, size, and distance to free surface. Using a finite-element-modeling framework, 120 tensile specimens with statistically similar pore networks were simulated (virtually tested) to failure. The pore networks were characterized by the proposed VDF, which was then compared to the nominal location of fracture (defined as the fracture-initiation location corresponding to the dominant crack responsible for final rupture). The location of maximum VDF accurately predicted the fracture location (within ± 0.2 mm) for 91 (76%) of the 120 samples and proved to be a more reliable indicator than the location of maximum reduced cross-section area and the location of largest pore diameter for predicting fracture location. Furthermore, the maximum VDF value was found to be more highly correlated than fraction porosity, pore size, reduced-cross section area, and total number of pores to the ultimate tensile strength, elongation, and toughness modulus.

J. M. Erickson · A. Rahman · A. D. Spear (✉)
University of Utah, Salt Lake City, USA
e-mail: ashley.spear@utah.edu

Keywords Porosity · Computational fracture mechanics · Ductile fracture · Finite-element modeling · Additive manufacturing

1 Introduction

Internal pores, also referred to as voids or defects, exist in most engineering materials (Huang and Gong 2018; Hogan et al. 2016; Sholl and Lively 2015; Chen et al. 2013; Varna et al. 1995). Metals are particularly prone to developing a significant number of pores, often referred to as pore networks or structures. Depending on the manufacturing process, pore sizes can range from undetectable to mms in diameter (Gunasegaram et al. 2009). In many cases, the mechanical performance of metal components containing pore networks differs significantly from their purely dense counterparts (Li et al. 2019; Voisin et al. 2018). In 1977, Gurson (1977) developed plastic-yield criterion for ductile porous materials. Since then, many other studies have expanded upon the Gurson model and have provided additional insight into the impact pores have on mechanical properties of metals (Cao et al. 2015; Fritzen et al. 2012; Khdir et al. 2015; Tvergaard 1981). However, each of these models, including the Gurson model, predicts mechanical properties assuming the pore network is homogeneous. While these models are widely used, they are unable to predict mechanical properties influenced by localized stress and strain from inhomogeneous pore networks. The need to pre-

dict mechanical properties using localized metrics that apply to both homogeneous and inhomogeneous pore networks becomes imperative given that components with pore networks (e.g., additively manufactured components) are being employed in critical applications.

One of the leading factors in the failure and fracture of porous ductile materials is the growth and coalescence of pores (Eichhubl and Aydin 2003; Kabatova et al. 2009; Tvergaard 1989). In a recent study by Kramer et al. (2019), in which tensile samples were imaged using micro-computed tomography (micro-CT) and mechanically loaded to failure, it was observed that voids encouraged and influenced both crack initiation and crack growth. However, the authors in that work were unable to find a definitive connection between the pores and global mechanical behavior. It was discussed that the ambiguous connection could be due to pores not being the primary driver of mechanical behavior and that other factors, such as surface roughness or geometry, likely played a role.

While many factors (e.g., surface roughness, thermal history, residual stresses) contribute to the difficulty in predicting the failure properties of porous materials, one possible explanation could lie in the lack of physical descriptors that adequately characterize pore networks. Over the years, porous materials have often been characterized solely by measuring the percentage of void volume relative to nominal volume, also known as void volume fraction or fraction porosity (Antou et al. 2004). In recent years, the advancement of imaging tools, such as micro-CT, has made it possible to map non-destructively the shape, size, and location of individual pores comprising a three-dimensional pore network. The availability of three-dimensional information has enabled new ways to characterize pore networks other than the traditional fraction porosity method. For example, Madison et al. (2018) performed an experimental study in which the pore networks of additively manufactured specimens were characterized by the following descriptors: total number of defects, average nearest-neighbor distance, average equivalent spherical diameter, maximum reduction of cross-sectional area, total pore volume, and maximum pore size. They correlated the pore network descriptors to elastic modulus, yield strength, ultimate strength, and elongation. When correlating yield strength to the pore network descriptors, they discovered that the total number of defects had a higher correlation value than total pore volume, which is analogous to fraction porosity. From that study, it was demonstrated that other types of physical descriptors, especially the number of defects, can play a more significant role in relating to the mechanical response than fraction porosity.

Works like those by Madison et al. (2018) and Kramer et al. (2019) show that pores can play a critical role in influencing the mechanical response of structural materials. However, it is still unknown to what extent pore networks impact mechanical properties (namely, fracture-related properties) and whether the current physical descriptors, like reduced cross-section area or maximum pore size, characterize pore networks adequately enough to predict the full mechanical response up to failure. In light of this knowledge gap, the objective of this work is two-fold: (1) to isolate the effect of pore networks on mechanical response to failure through virtual tension experiments performed using finite-element modeling, and (2) to establish a new metric to better characterize pore networks than existing metrics reported in the literature. For the latter objective, we present a void descriptor function (VDF) that accounts for pore connectivity, spacing, size, and position relative to free surface. Compared to commonly reported pore descriptors in the literature, the VDF is shown to correlate more strongly with toughness modulus, ultimate tensile strength, elongation, and location of final fracture (defined as the fracture-initiation location corresponding to the dominant crack responsible for final rupture).

2 Methods

In this study, 120[1] models (virtual tensile specimens) were created in Abaqus 6.14 (Smith 2014) with pore networks statistically similar to those in additively manufactured specimens. The tensile specimens were virtually loaded to failure using an element-deletion method, after which the stress–strain response and mechanical properties were extracted. The mechanical properties of the specimens were then correlated to pore network descriptors, including metrics commonly reported in the literature and the proposed VDF.

An overview of the entire computational framework is shown in Fig. 1. First, a pore network is defined

[1] The value of 120 was selected based on a formula from (Bellera and Hanley 2007), which is detailed further in Sect. 2.4.

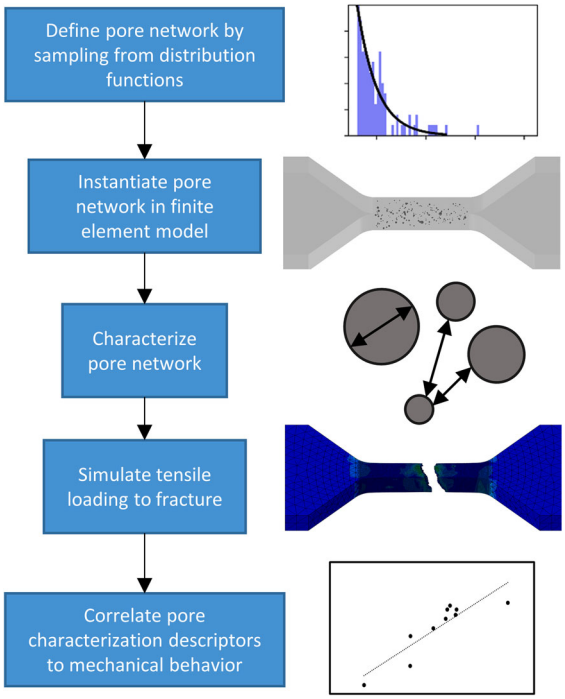

Fig. 1 High-level overview of study

by sampling from distributions of experimentally measured pore statistics. Second, a finite-element model is instantiated with the statistically generated pore network. Third, the pore network features are characterized using metrics found in literature, as well our new VDF descriptor. Fourth, the finite-element model is virtually tested to failure by tensile loading. Lastly, correlation analyses are performed to compare the relative correlations between the different pore descriptors and various mechanical properties. As a demonstration of the applicability of the VDF, linear regression models are trained and tested to predict failure properties as a function of the VDF metric.

2.1 Pore network definition and sampling strategy

In reality, pore networks found in engineering materials are complex and challenging to model explicitly. A pore network can be open, meaning that the majority of the pores are interconnected, and the structure is therefore permeable; alternatively, a pore network can be closed, meaning the pores are isolated and independent of one another. In either case, pores come in a variety of shapes, sizes, locations, and inter-connectivity. To simplify the modeling of these complex pore networks, we elected to model a closed-pore network, idealizing the pores as spheres.

Rather than randomly generating pores within each sample, we seek to generate pore networks that are statistically similar to pore networks resulting from common manufacturing processes. For this, we obtained experimental-characterization data from Sandia National Laboratories, in which pore networks of additively manufactured specimens were determined by micro-CT scans (Boyce et al. 2017). Using the micro-CT data, probability distribution functions were fit to the number of pores found in each specimen (Fig. 2a) and to the pore diameters (Fig. 2c). Out of eight types of distributions considered, the gamma distribution function (Hogg et al. 2012) was found to provide the best fit for both pore count and pore diameter. The shape and scale factors used for pore-count distribution were 1.67 and 70.9, respectively, and for pore-diameter distribution, the shape and scale factors were 1.00 and 0.0195, respectively. Note that the smallest pore diameter considered for explicitly modeling a pore network was 0.03 mm. This threshold was used to exponentially reduce the number of elements needed to represent a pore network in a finite-element model while still retaining the majority of pores that are resolvable by most lab-scale micro-CT systems. For each model generated, we first sampled from the distribution representing the pore count to determine how many times we would need to sample from the distribution representing the pore size. Figure 2b, d show sampled model data from the fitted gamma distribution. The centroidal coordinates of the pores were sampled uniformly from the respective ranges of x $[-2.0, 2.0]$, y $[-0.5, 0.5]$, z $[-0.5, 0.5]$, corresponding to the limits (in mm) of the length, width, and depth, respectively, of the specimen gauge region. Pores that overlapped with others were re-sampled using the Monte Carlo method (Su et al. 2010). This was done to ensure a closed-pore network in which each pore was independent of the other pores and spherical in shape. Figure 2e, f provide a qualitative visual comparison between experimental and synthetic pore structures.

2.2 Pore network characterization

As described in Sect. 2.1, pore networks are a challenge to characterize due to their high dimensionality. A sin-

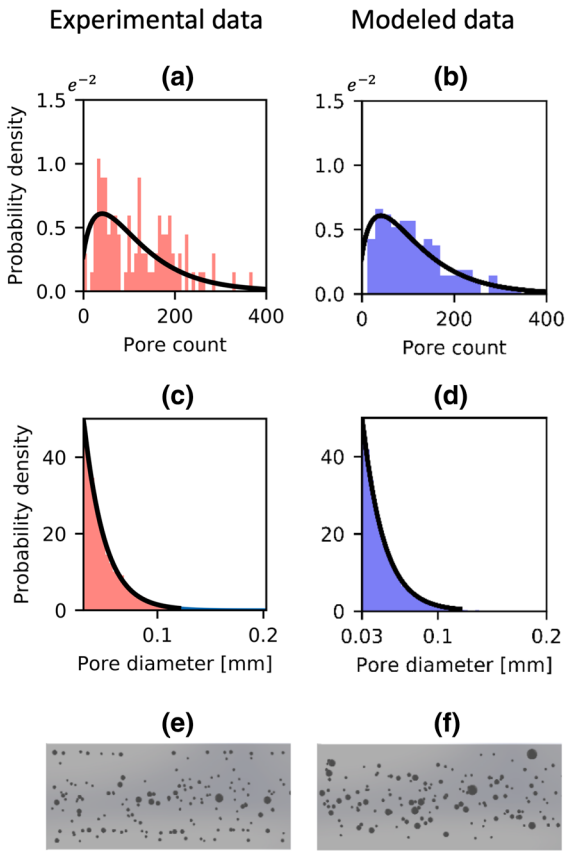

Fig. 2 Pore-sampling technique based on a subset of additively manufactured specimens from Ref. (Boyce et al. 2017): **a** probability density based on number of pores found in each sample, with fitted gamma distribution; **b** sampled data from gamma distribution fitted to pore count; **c** probability density based on pore diameters found in experimental specimens, with fitted gamma distribution; **d** sampled data from gamma distribution fitted to pore diameters; **e** example of experimentally characterized 3D pore network; **f** example of modeled 3D pore network

gle pore network can contain hundreds to thousands of pores, where each pore has a unique shape, size, position, and orientation. Fraction porosity has provided an intuitive and easy-to-measure metric to overcome this challenge (Slotwinski et al. 2014). However, fraction porosity is a global characteristic of the pore network and does not provide information regarding the arrangement of pores. For example, two samples with the same fraction porosity could have different arrangements of pores, resulting in different mechanical responses, as shown by Orsini and Zikry (2001). Thus, to adequately characterize a pore network, pore arrangement should also be used in the characterization technique.

2.2.1 Derivation of void descriptor function (VDF)

In the following, we present a method to characterize a pore network by incorporating volume and the spatial distribution of pores into a single function. The derivation of the function is inspired by a Laplace radial distribution function used in the work by von Lilienfeld et al. (2015), which derived a Fourier descriptor function to represent atomic external potential as a function of atomic distances. In general, radial distribution functions are used in molecular dynamics to describe the density of atoms as a function of distance from a reference point (Lyubartsev and Laaksonen 1995; Levine et al. 2011). Similarly, our proposed function describes the density of void volume as a function of position.

First, assuming spherical pores, we begin by defining the variables that parameterize a pore:

$$P_i = [v_i, d_i, x_i, y_i, z_i], \tag{1}$$

where P_i refers to a single pore that has the attributes of pore volume (v_i), diameter (d_i), and centroid location (x_i, y_i, z_i). The pore network is defined by:

$$\mathbf{P} = \begin{bmatrix} v_1 & d_1 & x_1 & y_1 & z_1 \\ v_2 & d_2 & x_2 & y_2 & z_2 \\ \vdots & \vdots & \vdots & \vdots & \vdots \\ v_n & d_n & x_n & y_n & z_n \end{bmatrix}, \tag{2}$$

where $\mathbf{P}$ is an array of pore attributes of length n, and n is the total number of pores in the specimen (or volume of interest).

The governing form of the VDF is rooted in the definition of fraction porosity, where porosity is defined by the summation of pore volume normalized by the ideal reference volume, V_{ref}:

$$Porosity = \sum_{i}^{n} \frac{v_i}{V_{ref}}. \tag{3}$$

Using Eq. 3 as our foundation, we express porosity as a function of x_{ref}, a reference position along the axial direction of the tensile specimen, to signal positions that are highly populated by pores. In the literature, it is shown that pore clustering and pores close to the free

surface have a significant influence on the mechanical behavior of porous materials (Fan et al. 2003; Chawla and Deng 2005). With this in mind, we modify Eq. 3 to incorporate weighting functions of axial position (clustering) and distance to the free surface:

$$VDF(x_{ref}) = \sum_{i}^{n} \frac{v_i w_c(x_i, x_{ref}) w_{fs}(d_i, y_i, z_i)}{V_{ref}}, \quad (4)$$

where w_c is a weighting function that expresses the impact that pore i at axial coordinate x_i has on the point of reference, and w_{fs} is a weighting function that expresses the impact that pore i located a given distance to the free surface has on the reference point.

The requirements for these weighting functions are that they return values between 0 and 1, are symmetric about a reference point, and exponentially decay moving away from the reference point. While many functions exist that meet these requirements, a Laplacian distribution function is chosen due to both its adaptability and simplicity. The general form of the Laplacian is defined as,

$$Laplacian = f(x) = \frac{1}{2\beta} e^{-\frac{|x-\mu|}{\beta}}, \quad (5)$$

where μ is the location parameter, or in this case, the point of reference, and β is the scaling parameter.

Using the main function form of the Laplacian, we define our clustering weighting function for a given pore as follows:

$$w_c(x, x_{ref}) = \frac{1}{\alpha} e^{-\frac{|x-x_{ref}|}{\alpha L}}, \quad (6)$$

where α is the scaling parameter for the exponential decay and L is the length of the gauge region to normalize the distance. The parameter α controls the shape of the weighting function used to express the relative influence of a given pore based on its axial position with respect to the point of reference. A small value of α indicates a rapid decay; while a large value of α indicates a more gradual decay. This implies that a small value of α weights less significantly pores that are farther away (axially) from the point of reference compared to a large value of α. Similarly, we define the weighting function of pore position relative to a free surface as follows,

$$w_{fs}(d, y, z) = \frac{1}{\rho} e^{-\frac{|c-\frac{d}{2}-\sqrt{y^2+z^2}|}{\rho c}}, \quad (7)$$

where d is the pore diameter, y and z are pore coordinates that describe its radial distance from the center (neutral axis) of the gauge region, c is the maximum radial distance from the center (neutral axis) of the gauge region to the free surface, and ρ is the scaling parameter. Similar to Eq. 6, the weighting parameter ρ controls the rate of decay used to express the relative influence of a given pore based on its radial position (in the y-z plane) with respect to the free surface of the specimen.

The final form of the VDF becomes:

$$VDF(x_{ref}, \mathbf{P}) = \sum_{i=1}^{n} \frac{v_i e^{-\frac{s_i}{\alpha L} - \frac{|c-r_i|}{\rho c}}}{V_{gauge}}, \quad (8)$$

where

$$s_i = |x_i - x_{ref}| \quad (9)$$

and

$$r_i = \sqrt{y_i^2 + z_i^2} + \frac{d_i}{2}. \quad (10)$$

Note in Eq. 8 that the coefficients that appear in Eqs. 6 and 7 ($1/\alpha$ and $1/\rho$, respectively) have been omitted from the VDF function. This is done to simplify the expression, as the VDF is not required to be a probability distribution function.

The purpose of the VDF is to identify positions along the gauge section that are highly populated by critical pore structures, thus signaling where fracture is likely to occur when mechanically loaded. To illustrate the definitions and implementation of the VDF, Fig. 3 shows a sample pore network. Figure 3c shows the variables defining the pore network, and Fig. 3b shows five points of reference at which the VDF is evaluated. Figure 3d shows a plot of the VDF along the axial direction of the gauge region. As shown in Fig. 3d, the maximum value of the VDF occurs at reference point x_4, which is hypothesized to be the approximate location of fracture. This hypothesis is explored further using computational fracture simulations, described in Sect. 3.2.

The scaling parameters in Eq. 8 can take on any positive, non-zero value. However, to optimize the pre-

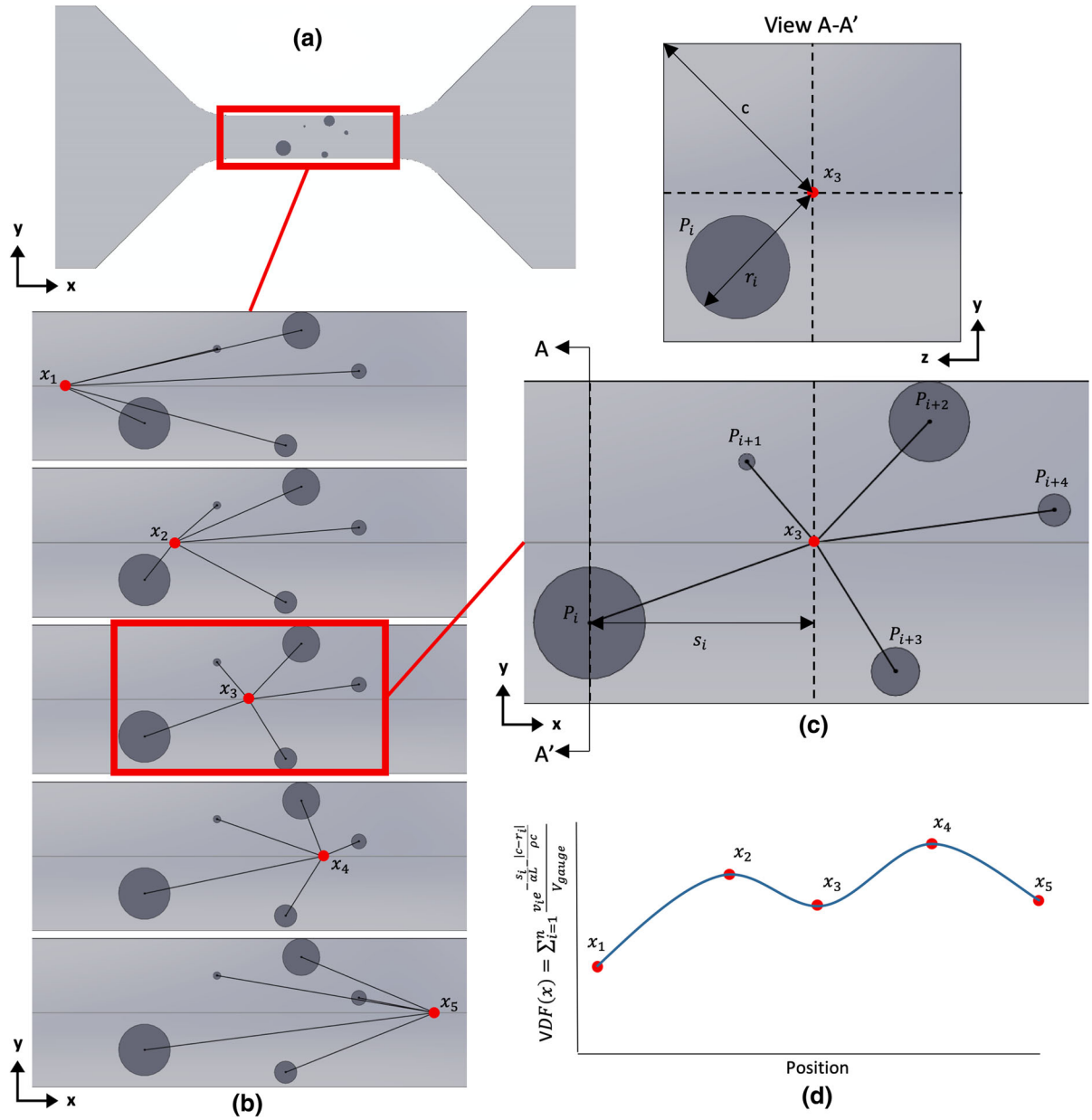

Fig. 3 Illustration of void descriptor function: **a** high-level depiction of a pore network inside a tensile specimen, **b** sequence of images showing a magnified view of the pore network with different points of reference along the x-direction, **c** detailed axial and cross-sectional views of the gauge section showing variables s and r used in VDF equation, and **d** plot of VDF values for the reference points along the x-direction

dictive capability of the VDF, the scaling parameters can be calibrated. To assess the sensitivity of the VDF-based predictions with respect to α and ρ, a study was performed on the 120 simulations (detailed in Sect. 3) in which the data set was randomly divided into three groups of 40 samples. For one group of 40 samples, the scaling parameters were optimized such that maximum correlation was achieved between the location of the VDF global maximum and the actual location of fracture among the 40 samples. The optimization was performed using a Bayesian optimization technique (Shahriari et al. 2016). Then, using the scaling

Table 1 List of pore network characterization descriptors with their corresponding name, variable, units, and description

Characterization descriptor	Variable	Units	Description
Fraction porosity	V_{fract}	%	The percent of pore volume to nominal volume
Number of pores	N_{tot}	count	The total number of pores in gauge region of sample
Average cross-section area reduction	CSA_{avg}	%	The average percent of area missing from nominal cross-section area
Max. cross-section area reduction	CSA_{max}	%	The maximum percent of area missing from nominal cross-section area
Max. cross-section area reduction location	$x_{CSA,max}$	mm	Axial location of the max cross-section area reduction
Average nearest neighbor distance	NND_{avg}	mm	The average distance to nearest neighboring pore
Average equivalent spherical diameter	ESD_{avg}	mm	The average diameter of all pores in the sample
Max. equivalent spherical diameter	ESD_{max}	mm	The maximum diameter of all pores in sample
Max. equivalent spherical diameter location	$x_{ESD,max}$	mm	Axial location of the maximum pore diameter
Max. VDF value	VDF_{max}	no units	The global maximum value of the VDF
Max. VDF value location	$x_{VDF,max}$	mm	Axial location of the VDF global maximum value

parameters optimized for the 40 samples, the VDF was evaluated for the remaining 80 samples and used to blindly predict the fracture locations. The process was repeated for the second and third sets of 40 samples, each time predicting fracture location for the remaining 80 samples. The results are presented in Table 5 of the Appendix. It is shown that a range of values for α and ρ results in a similar number of accurate predictions of fracture location in the blind assessments, suggesting that the predictive capability of the VDF depends primarily upon its functional form rather than on the specific values chosen for α and ρ. Thus, for the remainder of the manuscript, we chose to optimize the scaling parameters using the entire data set of 120 samples. The optimized values for α and ρ were found to be 0.220 and 0.188, respectively, which are used in all reported evaluations of the VDF throughout the remainder of the manuscript.

2.2.2 Pore-network characterization variables

Along with developing a new pore network descriptor, we aim to compare the relative performance of the VDF to pore-related metrics commonly reported in the literature in terms of ability to predict ductile-metal failure properties. The pore-related metrics considered include the following: fraction porosity, maximum percent reduction of cross-sectional area, average percent reduction of cross-sectional area, total pore count, average distance to nearest neighboring pore, average equivalent pore diameter, and maximum equivalent pore diameter. Maximum percent reduction of cross-sectional area and maximum equivalent pore diameter also have associated locations, which will be used to correlate with the dominant fracture location. A list of all the pore-related metrics with their definitions is provided in Table 1.

2.3 Finite-element models

Abaqus 6.14 was used to simulate tensile loading to failure of all 120 porous specimens. An isotropic elastic-plastic constitutive model with von Mises plasticity and material hardening was used. Due to the nonlinearity of the stress–strain response, the simulation was divided into three phases: elastic, plastic, and progressive damage, or material softening. The elastic response is defined by the material's elastic modulus and Poisson's ratio. The plastic response is defined by plastic yield stress versus strain. The progressive damage is defined by fracture strain, stress triaxiality, strain rate, and fracture energy. The calibration procedure and final properties for each phase are detailed in subsequent sections.

2.3.1 Geometry

The tensile sample geometry in this study is the same nominal geometry used by Boyce et al. (2017), which is based on the ASTM E8 standard (Standard ASTM, E8, E8M-13a 2013). Figure 4 shows the dimensions of

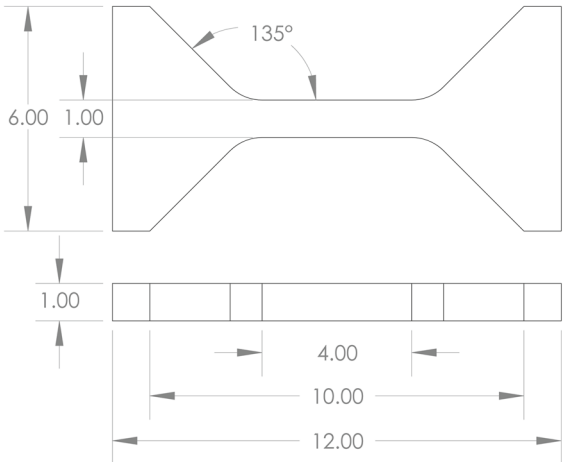

Fig. 4 Dimensions of specimen geometry. All units in mm

the sample. The gauge region is 4 mm long with a 1×1 mm^2 cross-section area.

2.3.2 Material properties

The material properties were calibrated from additively manufactured (AM) 17-4 PH stainless steel experimental data (Boyce et al. 2017). The data set consists of 109 AM samples with low porosity pore networks that are qualitatively and quantitatively similar to the pore networks generated in our study. From the 109 samples, the average unloading elastic modulus was found to be 182 MPa; however, we opted to use the industrial-based elastic modulus of 196.6 MPa to avoid double counting the effects of pores from the experimental data. To calibrate the plastic and fracture properties, we used four samples that were considered to nominally represent the stress–strain behavior of the entire data set. The precise pore networks for the four samples were modeled in Abaqus 6.14, and the hardening and damage properties were iteratively modified to fit the finite-element stress–strain response to the experimental stress–strain response. To assist in the calibration of the hardening properties, we used Abaqus' inbuilt calibration tool to convert engineering stress–strain to true stress–strain. This relationship only holds true up to necking or softening of the material. Subsequently, the true stress–strain data and fracture properties were fine-tuned until the finite-element model results matched experimental stress–strain data. The true plastic stress–strain used is shown in Fig. 5. Additionally, a condensed tabular input is provided in Table 6 in the Appendix. The fracture

Table 2 Material properties used for all 120 finite-element models

Material property	Units	Value
Elastic modulus	MPa	196,600
Poisson's ratio		0.3
Density	kg/m^3	8000
Fracture strain	mm/mm	0.2
Stress triaxility	MPa/MPa	0.33
Strain rate	strain/sec	0
Fracture energy	mJ	0

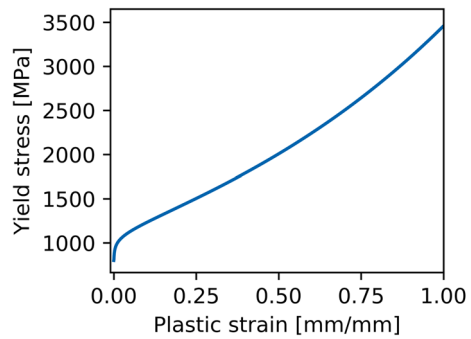

Fig. 5 Yield stress response as a function of plastic strain. Abaqus input data to model true stress–strain response

energy was chosen to be 0, which resulted in very little softening behavior prior to final rupture (i.e., an abrupt decrease in the stress–strain curve). This was consistent with the stress–strain behavior observed in the experimental data provided by Sandia National Laboratories (Boyce et al. 2017). The strain rate was set to 0, making the simulation independent of strain rate effects. The fracture strain was found to be 0.2 based on matching the simulation elongations to the experimental elongations for the four calibration specimens. A summary of the material properties is shown in Table 2 and Fig. 5.

2.3.3 Boundary conditions

The boundary conditions were modeled to emulate the experimental testing conditions. Displacement constraints were applied to the leading faces of the grips, which are highlighted in red in Fig. 6a. The left grip faces shown in Fig. 6a were fixed in the x, y, and z directions, and the right grip faces were fixed in the y and z directions, with 1 mm smooth displacement step applied in the x-direction. A smooth displacement

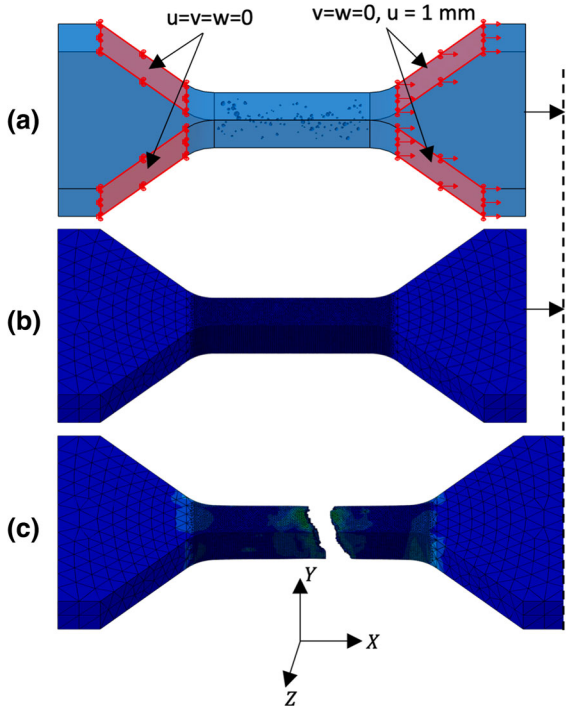

Fig. 6 Boundary conditions of finite-element model: **a** boundary conditions applied at the leading faces of the grips; **b** meshed, undeformed specimen; and **c** fractured specimen at end of 1 mm applied displacement

step slowly ramps up and down the displacement rate at the beginning and end of the simulation to mitigate dynamic-inertia effects. To ensure a quasi-static response, an average displacement of 1.54 mm/s was used. The displacement of 1 mm was determined to be sufficient to induce complete rupture of all specimens. Figure 6b shows a sample state and mesh before loading. Figure 6c depicts complete fracture in the fully deformed state at the end of 1 mm displacement.

2.3.4 Element deletion

An element-deletion approach was chosen to represent fracture because of its computational efficiency, ability to initiate fracture without defining crack initiation locations *a priori*, and the authors' prior experience applying the method in the Third Sandia Fracture Challenge (Kramer et al. 2019; Spear et al. 2019). In the element-deletion method, an element is deleted (element stiffness is reduced to 0) when it reaches user-specified criteria of either strain or energy. Consequently, fracture can occur anywhere in the model that reaches the specified criteria. This is a favorable method to test the variations of fracture location and mechanical properties influenced by a specimen's unique arrangement of pores.

The primary disadvantage of using element deletion is mesh sensitivity. For an element to be deleted from a simulation, the progressive damage variable governed by plastic strain needs to reach 1.0. The rate of progressive damage is slower in larger elements compared to smaller elements. Due to the dependence of progressive damage on element size, simulations could exhibit mesh-related artifacts and inconsistencies among simulations. To mitigate this problem, an effort was made to ensure that the element sizes were uniform throughout the gauge region and consistent among all 120 models. Thus, we chose an element size that could adequately conform to the smallest pore size found among the simulations, while also ensuring that the mechanical properties (ultimate tensile strength, elongation, toughness modulus, and fracture location) were converged with respect to mesh size. A mesh convergence error less than 1% was achieved for ultimate tensile strength and fracture location, while elongation and toughness modulus had a convergence error of 4%, which was deemed to be acceptable. The final element size used within the gauge region for all models was 0.05 mm.

The numerical simulations were performed using the Abaqus 6.14 explicit solver. A mass scaling factor of 1,000,000 was used to decrease simulation time. This factor was applied consistently across all simulations, and no impact on the mechanical response was observed when comparing the mechanical response to simulations without mass scaling. The simulation time was approximately 790 CPU hours for each sample using 32 parallel processors through the University of Utah's Center for High Performance Computing (CHPC). Approximately 95,000 CPU hours were required to simulate failure of all 120 models.

2.3.5 Post-simulation processing

Stress–strain curves were generated by extracting force and displacement data from each simulation. In each finite-element model, two partitions were embedded in the ends of the gauge region and defined as element sets, namely, "Fixed" and "Displaced." From

Table 3 List of mechanical properties with their corresponding name, variable, units, and description

Mechanical property	Variable	Units	Description
Elastic modulus	E	GPa	Slope of elastic region in stress–strain curve
Yield strength	σ_y	MPa	Stress value at which plastic yielding begins, offset by 0.2% strain
Ultimate tensile strength	σ_u	MPa	Maximum stress value in stress–strain curve
Percent elongation	e_f	%	Value of strain at fracture multiplied by 100
Toughness modulus	U_F	MPa	Total energy dissipated during tensile loading (area under stress–strain curve)
Fracture location	x_{fract}	mm	Axial location in gauge region where dominant crack initiates

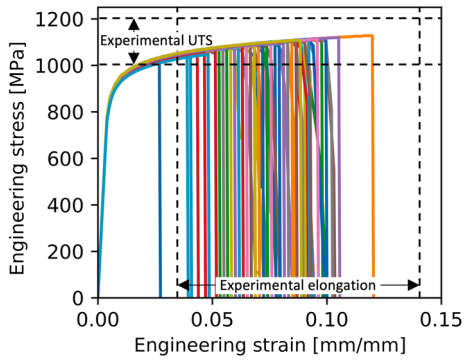

Fig. 7 Stress–strain data for all 120 finite-element simulations. Experimental bounds from Ref. (Boyce et al. 2017) are included for reference

the "Fixed" element set, the reaction forces were summed across the elements and divided by the nominal cross-section area of 1.0 mm^2 to calculate the engineering stress. Engineering strain was calculated as the change in length of the gauge section divided by the original gauge length of 4.0 mm. From the engineering stress–strain plot, the mechanical properties of elastic modulus, yield strength, ultimate tensile strength, toughness modulus, and elongation were determined. Additionally, the location of fracture (defined as the fracture-initiation location corresponding to the dominant crack responsible for final rupture) was recorded. Table 3 provides a summary of all mechanical properties and attributes recorded for each simulation.

2.4 Correlation analysis and regression model

To assess the relative performance of the VDF compared to commonly reported pore-related metrics in terms of characterizing pore structures and their relationships with mechanical behavior, correlation and regression analyses were carried out. First, to ensure that the correlation results would be statistically significant, a sample size was determined using a formula derived by Bellera and Hanley (2007). The formula estimates the minimum sample size needed to satisfy requirements for a specific confidence interval and margin of error given that the data are either uniformly or normally distributed. Thus, for a 90% confidence interval and a 10% margin of error, it was estimated that 120 pore instantiations would be required to achieve statistically significant correlation results. After collecting data for all 120 simulations, two sets of Pearson correlation coefficients were calculated: (1) between simulated mechanical properties and non-location-specific pore metrics, including the maximum VDF value, and (2) between simulated fracture location and location-specific pore metrics, including the location of the maximum VDF value.

Additionally, to demonstrate the predictive capabilities of the VDF metric, regression analyses were performed between either the maximum VDF value or its location and the resulting mechanical properties or location of fracture, respectively. The results are compared to regression analyses performed using other commonly reported pore-related metrics. Note, the objective of this work is not to develop a predictive model; rather, we aim to demonstrate the applicability of the VDF metric and relative performance through direct comparison with other metrics. For that reason, and for illustration purposes only, we assume a linear regression model. Each model was trained using 80% of the simulation data (96 samples) and tested using the remaining 20% of the simulation data (24 samples). The analysis was similar to regression studies performed on the mechanical properties of

Table 4 List of the minimum, maximum, and average mechanical property values from finite-element simulation and experimental data

Mechanical Property	Simulation data			Experimental data (Boyce et al. 2017)		
	Min	Max	Mean	Min	Max	Mean
E [GPa]	193	198	197	164	206	182
σ_y [MPa]	866[a]	900[a]	897[a]	770[b]	1142[b]	924[b]
σ_u [MPa]	1013	1128	1090	1005	1212	1085
e_f [%]	2.73	12.0	7.46	3.47	14.0	8.18
U_F [MPa]	23.7	125	74.4	na		
x_{fract} [mm]	−1.88	1.74	−0.05	na		

[a] Yield strength calculated using 0.2% offset
[b] Yield strength calculated using 0.5% offset

cement (Jahed Armaghani et al. 2015; Khademi et al. 2016).

3 Results and discussion

3.1 Finite-element-based fracture simulations

Figure 7 presents the stress–strain curves from which the mechanical properties were extracted for all 120 finite-element simulations. The minimum, maximum, and average mechanical properties among all simulations are reported in Table 4, along with the corresponding mechanical properties from the experimental data (Boyce et al. 2017) [2]. Based on the data presented in Table 4, it is apparent that the simulation data underpredicts the range of values for elastic modulus and yield strength compared to the experimental data. However, the range of values for ultimate strength and percent elongation from the numerical simulations closely represent those from the experimental data. The small range of values for elastic modulus and yield strength from the simulations is explained by the fact that the only source of variability within the models is the pore structure (not constitutive properties), which does not manifest in significant variability in the stress–strain response until onset of fracture.

Figure 8 shows the final fractured specimens for nine representative fracture scenarios of the 120 test cases. Along with each image of a fractured model is a plot of the VDF, evaluated along the gauge region for the corresponding sample. For comparison, the plot also includes the percent reduction of cross-sectional area evaluated along the gauge length. A vertical line in each plot indicates the nominal location of fracture within each specimen. One of the benefits of the VDF metric versus the percent cross-section area reduction metric is that the former is far less noisy than the latter, as evident in the plots of Fig. 8. This is due to the continuous nature of the VDF; whereas, the percent cross-section area reduction is much more sensitive to highly localized changes in pore structure. Consequently, the VDF provides a stronger signal with less noise and, in most cases, an obvious global maximum. The second point of interest is that the location of the VDF global maximum coincides with the nominal location of fracture for a majority of the samples (91 out of 120). Representative examples are shown in Fig. 8a–f. Additionally, in the majority of cases for which the VDF global maximum does not coincide with the fracture location, a local maximum[3] does coincide with the fracture location, exemplified in Fig. 8g, h. This discovery is significant in that it suggests that, in many cases, the location of fracture can be predicted *a priori* based solely on the pore network, which is discussed in greater detail below. It is worth noting that there are some cases (6 out of 120, based on a 5% error tolerance) for which there does not appear to be an obvious relationship between the VDF value and the location of fracture, as illustrated in Fig. 8i. However, such cases are rare and merit further investigation.

[2] The stress data reported in Ref. (Boyce et al. 2017) were based on width and thickness measurements for individual tensile samples using a Keyence IM-6225T optical measurement system and Mitutoyo Digimatic Micrometer, respectively.

[3] The built-in function scipy.signal.find_peaks in SciPy v1.4.1 was used to identify all local maxima.

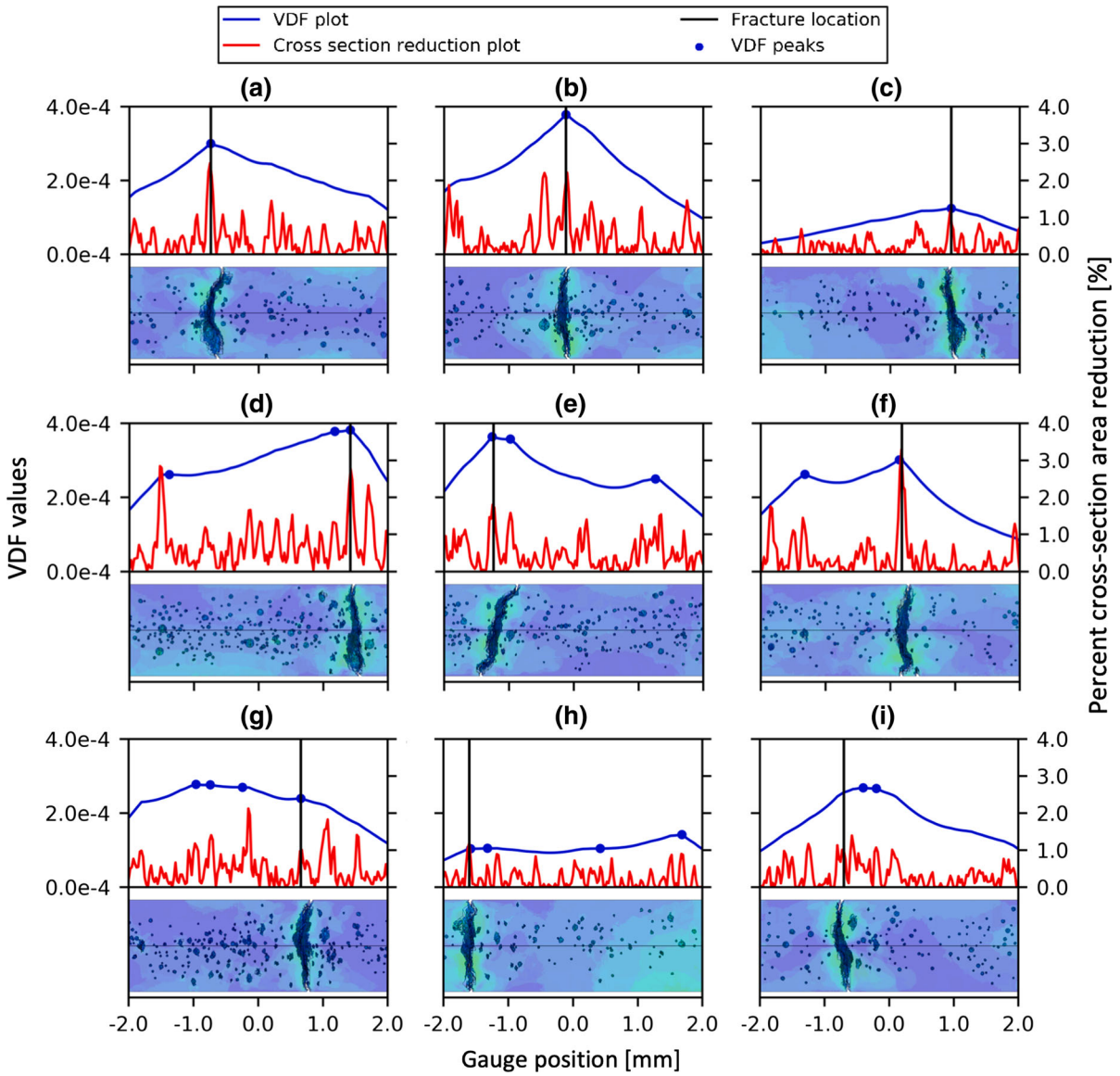

Fig. 8 A comparison between VDF, percent cross-section area reduction, and fracture location in nine representative samples: **a–f** samples for which the fracture location aligned with the global maximum of the VDF; **g–h** samples for which the fracture location aligned with a local maximum of the VDF; and **i** a sample in which the fracture location did not align with either global or local maxima of the VDF. Translucent views of the von Mises stress fields are overlaid to highlight the locations of final fracture (these are taken after rupture for visual purposes only, so stress legends are intentionally excluded)

3.2 Ability of the void descriptor function to predict fracture location

The ability of the VDF to predict fracture location is explored further here. The location of the VDF global maximum for each pore instantiation is compared directly to the nominal fracture location for each of the 120 samples, and a prediction error is calculated by taking the absolute distance between the fracture location and the global maximum VDF value location and dividing by the length of the gauge region. The frequency of accurately predicting fracture location based

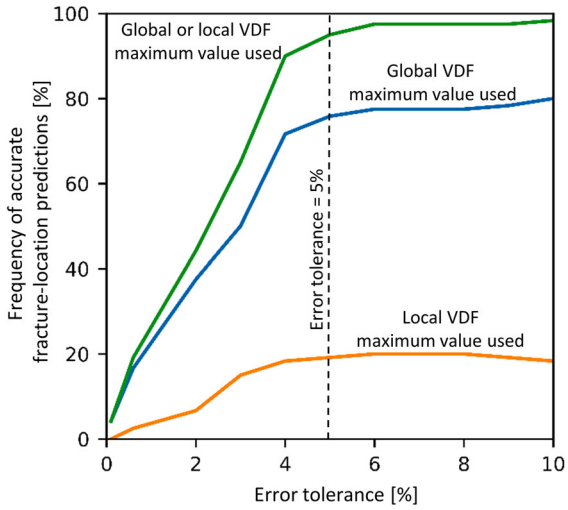

Fig. 9 Percentage of samples for which the location of VDF maxima accurately predict fracture location within a given error tolerance

on the VDF is plotted as a function of error tolerance in Fig. 9. The plot includes three curves: (1) cases for which the location of global maximum accurately predicts fracture location, (2) cases for which the location of a local (not global) maximum accurately predicts fracture location, and (3) cases for which the location of any maximum accurately predicts fracture location, i.e. the cumulative sum of the first two cases. The first case is considered to be the most impactful because of the unique signal of the predicted location. For example, Fig. 9 shows that the location of global maximum of the VDF accurately predicted 91 of the 120 samples, or 76% frequency, within a 5% error tolerance. The cumulative-sum curve shows that the fracture location will almost always occur at a location of maximum VDF, whether a local or global maximum, which is also useful information. In comparison to the other location metrics, the VDF predicted 91 samples, whereas the maximum cross-section reduction location and largest equivalent pore diameter location only predicted 58 and 59 samples, respectively (given a 5% error tolerance).

The certainty that the location of VDF global maximum will accurately predict fracture location can be determined based on the difference between global and local VDF maxima values. From this study, it is observed that when the VDF has a global maximum much greater than any local maxima, the fracture location will almost certainly coincide with the global maximum location. To quantify this observation, we introduce an ambiguity score calculated as follows:

$$AmbiguityScore = 1 - \frac{|VDF_{max_1} - VDF_{max_2}|}{VDF_{max_1}}, \tag{11}$$

where VDF_{max_1} is the global maximum, and VDF_{max_2} is the next greatest local maximum value. This measure helps classify the certainty of a VDF's predictive capability. For samples in which there is only one maximum, the ambiguity score is 0.0 and indicates that nominal fracture location will occur at the location of VDF global maximum. For samples in which the global and local maxima have similar values, the ambiguity score increases, and as a result, it is less certain that the fracture location will coincide with the location of global VDF maximum. Using this definition of ambiguity, the certainty of predicting fracture location based on VDF global maximum can be estimated, as illustrated in Fig. 10a–c. As shown by the curve labeled *Total number of samples* in Fig. 10c, there are 28 out of 120 samples (23%) that have a VDF ambiguity score of 0.0. As the VDF ambiguity score increases to 1.0, the total number of samples increases until all 120 are included. Likewise, we can plot the number of samples for which fracture location is accurately predicted within a 5% error tolerance as a cumulative function of ambiguity score. This curve is shown in red and is labeled *Number of accurately predicted samples*. As the ambiguity score increases from 0.0 to 1.0, the number of samples for which fracture location is accurately predicted increases from 28 to 91. The curve labeled *Percent of accurately predicted samples to total number of samples* represents the prediction certainty and is calculated by dividing the number of samples with accurate predictions of fracture location (red curve) by the total number of samples at or below a given VDF ambiguity score (blue curve). For example, at an ambiguity score of 0.7, the total number of samples with a VDF ambiguity score less than or equal to 0.7 is 39, of which 38 (97%) have fracture locations that are accurately predicted based on the location of VDF global maximum. This implies that, based on location of global VDF maximum, a design engineer could achieve above a 95% confidence level in predicting failure location for roughly one-third of the samples. In later sections, a VDF ambiguity score of 0.7 is referenced to select samples with high predictive certainty.

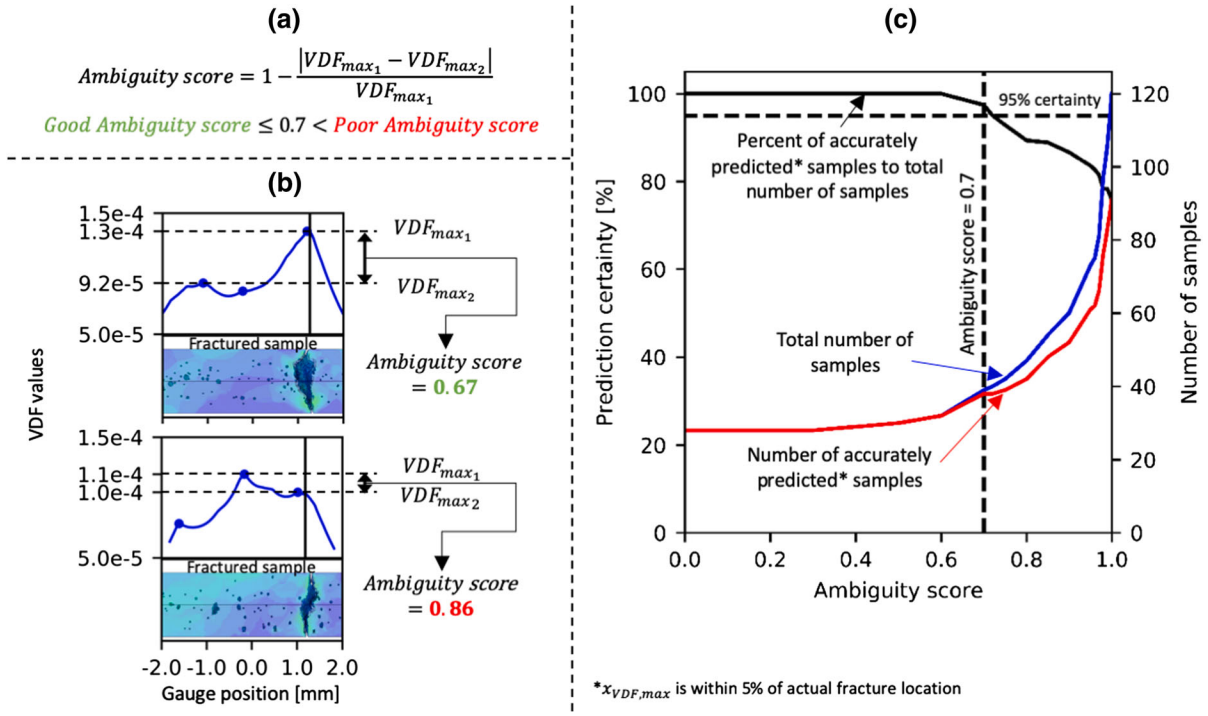

Fig. 10 Defining prediction certainty as a function of ambiguity score. **a** Definition of the transition point between a high and low ambiguity score. **b** Example of two VDF plots in which the ambiguity score is calculated. **c** A cumulative distribution of the number of samples with ambiguity scores at or below the value indicated on the horizontal axis

3.3 Correlation between pore-related metrics and mechanical response

Results from the Pearson correlation analyses described in Sect. 2.4 are presented in Fig. 11. Figure 11a presents the correlation coefficients between various mechanical properties and eight different pore-related metrics, including seven commonly reported metrics from the literature and the proposed metric of maximum VDF. As illustrated in Fig. 11a, the correlations with elastic modulus are actually stronger for three of the pore metrics (viz., fraction porosity, number of pores, and the average cross-section area reduction) than for the VDF_{max} metric. However, none of the Pearson correlation coefficients exceeds 0.7 for the elastic modulus, which represents the lowest overall set of correlation coefficients among all of the reported mechanical properties. This relatively low correlation can be explained by the lack of variability in elastic modulus among the 120 stress–strain curves shown in Fig. 7 and reported in Table 4. Similarly, the correlations between yield strength and fraction porosity, total number of pores, and the average cross-section area reduction are stronger than they are between yield strength and VDF_{max}. The strong correlation between number of pores and yield strength is in agreement with the experimental study by Madison et al. (2018), which found that the yield strength was highly correlated to the total number of pores in a sample. Furthermore, porosity has been shown in numerous studies to be highly correlated with plastic yielding (Gurson 1977; Tvergaard 1981; Hyun et al. 2001).

Interestingly, for all properties that are beyond yielding (viz., ultimate tensile strength, percent elongation, and toughness modulus), the VDF_{max} metric has the highest correlation among all eight pore-related metrics considered, suggesting that it could serve as a better indicator of fracture-related properties than other pore-related metrics reported in the literature. For example, the magnitude of the correlation coefficient between VDF_{max} and ultimate tensile strength is 0.878, followed by maximum cross-section area reduction,

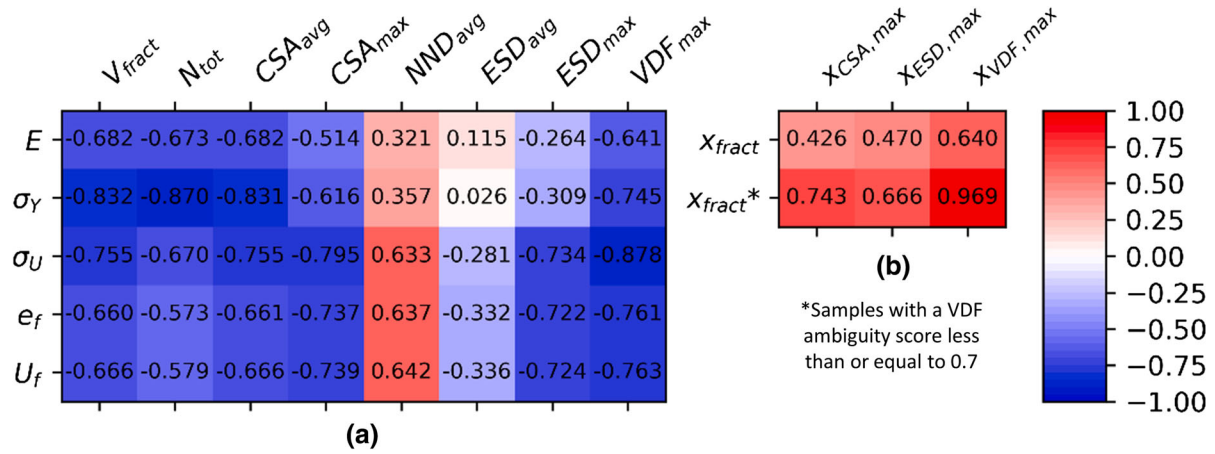

Fig. 11 **a** Pearson correlation coefficients between pore network descriptors (non-location-specific) and mechanical properties. **b** Pearson correlation coefficients associated with fracture location based on all samples in the data set (top row) and the subset of samples with an ambiguity score less than or equal to 0.7 (bottom row)

which has a correlation coefficient magnitude of 0.795. Unlike metrics like fraction porosity, pore count, and maximum pore diameter, the VDF_{max} metric accounts for pore clustering, which plays an important role in onset of fracture. Although metrics based on reduction of cross-sectional area and average nearest-neighbor distance account for pore clustering, to some extent, they do not account explicitly for the positions of pores relative to free surfaces, which is also known to influence onset of fracture. Pore clustering, size, and position relative to the free surface are all accounted for in the VDF metric.

Figure 11b presents the correlation coefficients between nominal location of fracture and locations of maximum pore-related metrics, including maximum cross-section area reduction, maximum equivalent spherical diameter of a pore, and VDF_{max}. There are two rows presented in the correlation matrix of Fig. 11b. The top row corresponds to a correlation analysis performed using all 120 samples in the data set. In that case, the locations of maximum cross-section area reduction and maximum equivalent spherical diameter have correlation coefficients with fracture location of just 0.426 and 0.470, respectively; whereas, the location of VDF_{max} has a correlation coefficient of 0.640. The second row in the matrix corresponds to a correlation analysis performed on the subset of samples that have a VDF ambiguity score less than or equal to 0.7 (see Fig. 10). Remarkably, in that case, the correlation between location of VDF_{max} and fracture location is 0.969, which is significantly greater than either of the other location-specific pore metrics and represents a near-perfect linear relationship. This relationship is explored further in the next section.

3.4 Regression analysis

To illustrate the predictive capabilities of the VDF-based metric, this subsection presents and discusses the results of linear-regression analyses performed between fracture-related properties and various pore metrics, including VDF_{max}, fraction porosity, location of VDF_{max}, location of maximum pore diameter, and location of maximum cross-section area reduction. Note, use of linear regression is not an assertion that the best-fit predictive model is linear. Rather, the purpose of performing linear regression is to illustrate the potential of the VDF as a variable in a predictive model and to provide a direct and simple comparison of its performance with that of other pore-related metrics.

Figure 12 presents a comparison between the performance of VDF_{max} and fraction porosity in terms of predicting ultimate tensile strength, toughness modulus, and elongation. For each pore metric, results are presented for both the training data and the testing data used in the regression analysis. For all three mechanical properties, and considering the performance for

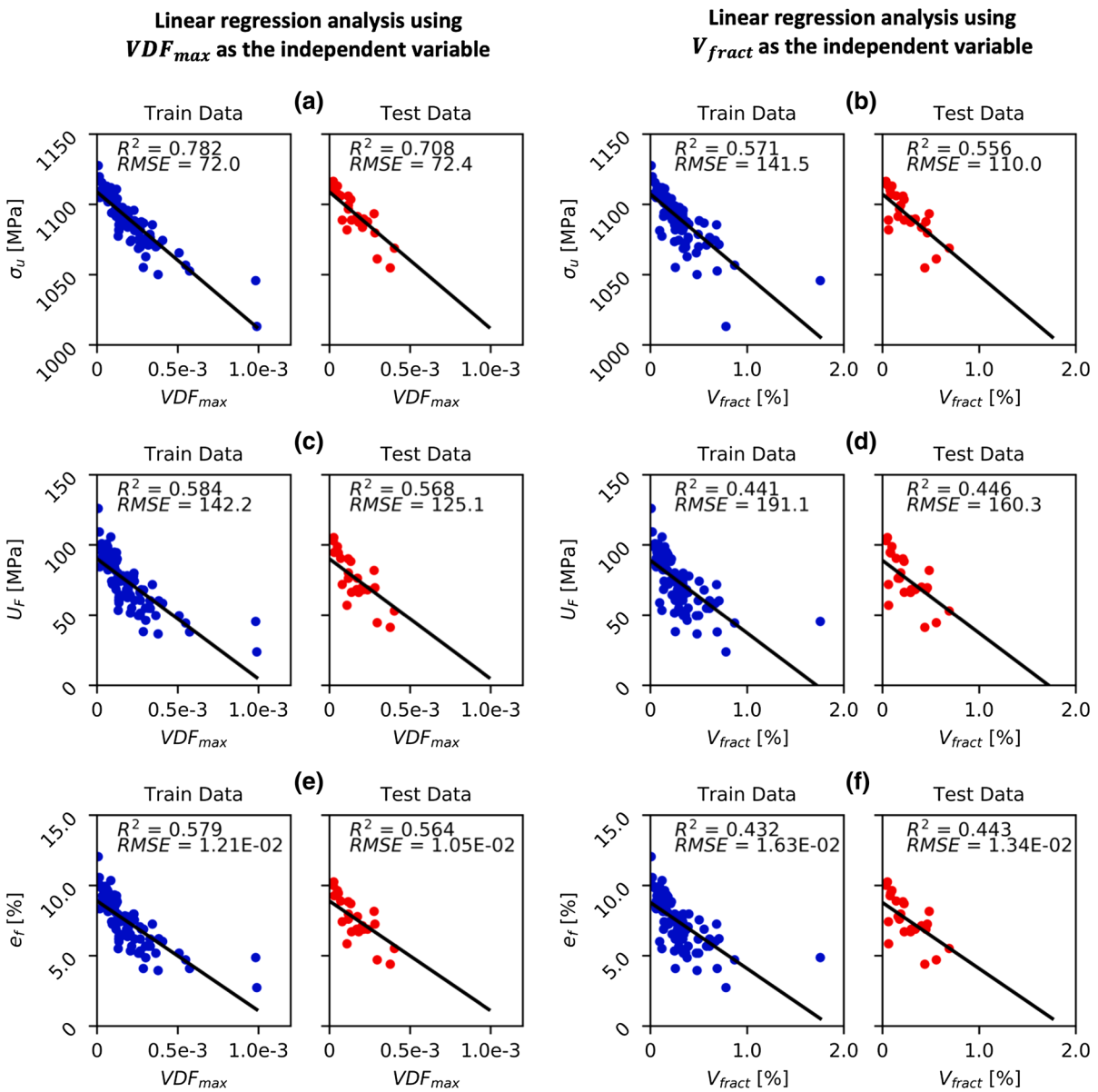

Fig. 12 Linear regression models showing ultimate tensile strength, toughness modulus, and elongation as functions of maximum VDF value (**a**, **c**, **e**) and fraction porosity (**b**, **d**, **f**)

both training and testing data, the VDF_{max} metric outperforms fraction porosity, as evidenced by both the R^2 and root-mean-squared error (RMSE) metrics. The best performing regression model is the ultimate tensile strength as a function of VDF_{max} (Fig. 12a), which results in R^2 values of 0.782 and 0.708 for the training and test sets, respectively. While these values are not ideal, they greatly outperform the regression model of ultimate tensile strength as a function of fraction porosity, as shown in Fig. 12b.

Figure 13 shows regression models of fracture location as a function of location of maximum VDF, location of maximum cross-section area reduction, and location of maximum pore diameter. Results from the regression analyses presented in Fig. 13 are divided

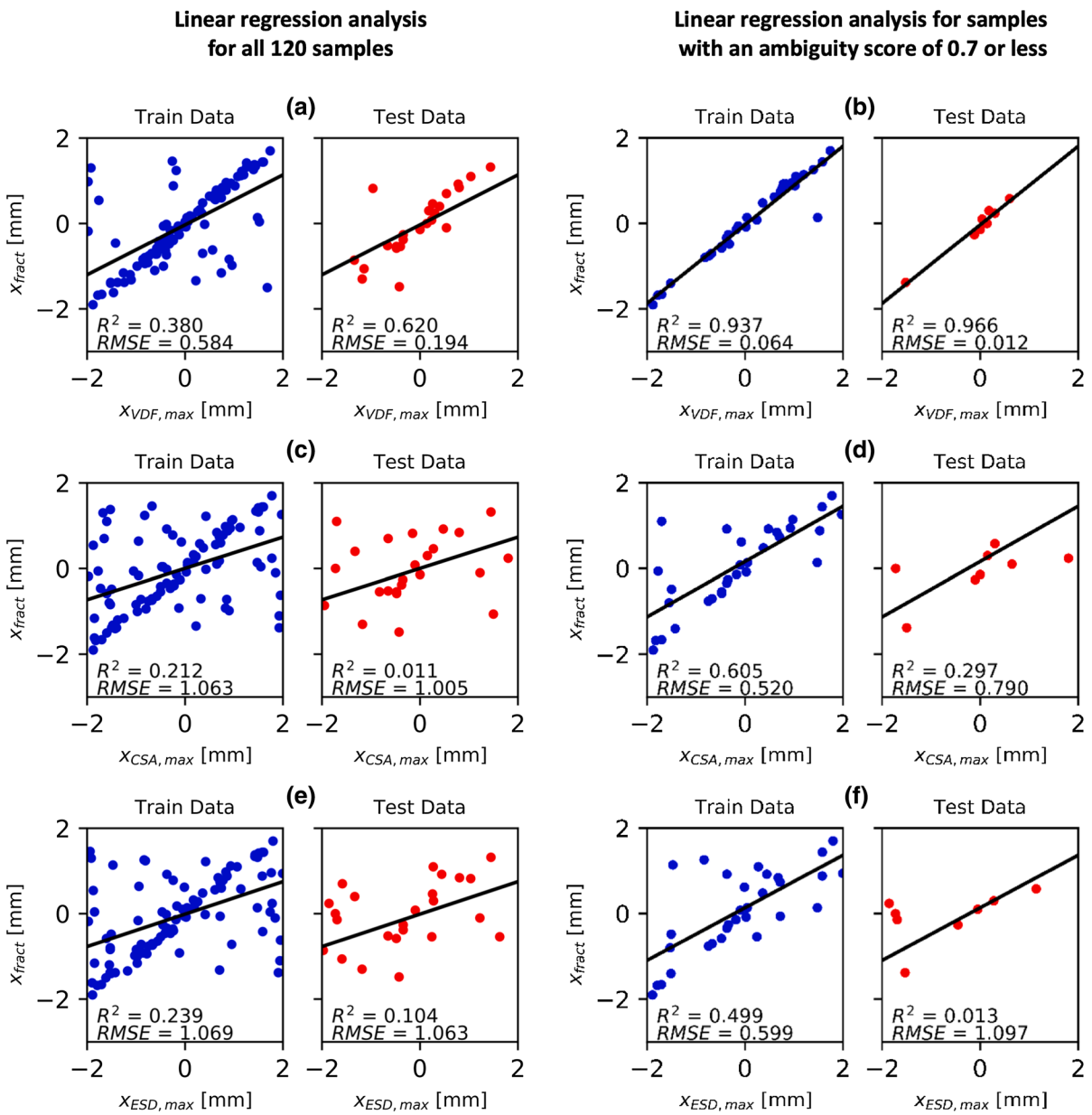

Fig. 13 Linear regression models showing fracture location as functions of location of maximum VDF value, location of maximum cross-section area reduction, and location of maximum pore diameter. **a**), (**c**), and (**e** use the entire data set. **b**, **d**, and **f** use a subset of the data corresponding to samples that have a VDF ambiguity score less than or equal to 0.7

into two cases: one that includes all 120 samples in the data set, and another that includes only the subset of samples that have VDF ambiguity scores less than or equal to 0.7 (see Fig. 10). Among the three pore-related metrics considered, the VDF-based metric outperforms the other pore-related metrics in terms of predicting nominal location of fracture. Figure 13a presents the regression model results based on location of VDF_{max} using all 120 data points in the set. While the R^2 values for the training and testing data in Fig. 13a are significantly greater than those corresponding to the other two pore metrics (Fig. 13c, e),

they are still not ideal (0.380 and 0.620, respectively). This is due, in large part, to the fact that the regression model does not account for cases in which a local, rather than global, VDF maximum accurately predicts the location of fracture. Thus, by restricting the data set to only those samples with an unambiguous maximum VDF value (i.e., those with an ambiguity score of 0.7 or less, presented in Fig. 13b), the R^2 values increase significantly to 0.937 and 0.966 for the training and test sets, respectively. This result is promising because it shows that, in many cases, the global maximum of the VDF function provides a clear and nearly perfect signal of the fracture location. Future efforts could consider how to incorporate into the fracture predictions cases where multiple, similar-valued maxima exist, which would further improve the predictive capability of the VDF.

3.5 Limitations, implications, and future work

There are several assumptions of the proposed VDF that merit further discussion. The first assumption is that all pores are spherical. This assumption was made for simplicity and was rationalized based on the typical pore shapes observed in additively manufactured materials (Rao et al. 2016). However, pore shape has been shown to influence mechanical behavior of porous materials (Cao et al. 2015; Khdir et al. 2015; Masmoudi et al. 2017). Thus, future modifications of the VDF could include an additional term to incorporate pore shape.

One of the objectives of this study was to isolate the effect of pore networks on the mechanical response under tensile loading; hence, the current VDF neglects the effects of surface roughness. Surface roughness has been found to be a crucial variable that influences the mechanical response of additively manufactured metals (e.g., see Ref. Watring et al. 2019), and in many real-world applications, surface roughness is expected to be present and to play a role in the mechanical behavior. Also, additively manufactured metals can exhibit anisotropic behavior with respect to build orientation. Thus, for future work, it would be important to include surface roughness into the VDF formulation and to consider the effects of anisotropy (if applicable), which would provide opportunities to perform VDF analysis directly on experimental data rather than strictly on idealized numerical data. Doing so would allow to assess the predictive capabilities of the VDF through experimental validation and blind prediction.

Another limitation of the VDF, in its current form, is that it is derived for one-dimensional problems. That is, the VDF is formulated as a function of x. The one-dimensional formulation is applicable to problems like the uniaxial tension tests studied here, where the nominal location of fracture can be adequately described by a single value of x. It is noted, however, that the current implementation of the VDF may inadequately weight pore-pore interactions in the y-z plane. For example, two pores with the same x coordinate would collectively have the same contribution to the VDF value whether those pores are located in close proximity to each other or on opposite sides of the neutral axis. The VDF formulation could, therefore, be enhanced by incorporating effects of pore-pore interactions in the y-z plane. Additionally, future work could seek to generalize the VDF to three dimensions to enable characterization of pore networks in more complex geometries and to signal fracture in any arbitrary location.

The synthetic pore networks modeled in this work were generated by sampling distributions of pore location and pore size. While the resulting pore structures are statistically representative of experimental observations, the modeled pore structures were not generated based on physical processes that govern the formation of specific pore structures. Thus, future research could focus on generating pore structures based on physics-driven modeling of the manufacturing process, which could provide a critical link between process, pore structure, and mechanical properties.

Despite the limitations described above, the work presented herein demonstrates that the VDF is a promising metric to assist with characterizing pore networks and predicting ductile-metal failure properties. The VDF improves upon existing pore-related metrics reported in the literature by accounting for pore clustering, pore size, and position of pores relative to free surfaces. In terms of potential applications, the VDF could be incorporated into a screening tool to aid in predicting, *a priori*, likely locations of fracture as well as post-yield mechanical properties of porous and ductile metals. For example, micro-CT images could be analyzed using the VDF (or a modified version thereof), providing valuable infor-

mation for part qualification. Another potential application of the VDF is as a parameter that could be incorporated into constitutive models, analogous to the incorporation of fraction porosity in the Gurson model to predict plastic yielding. An additional benefit of the VDF is that it is straight-forward to evaluate, which further enhances its attractiveness in application.

4 Conclusion

A void descriptor function (VDF) is derived to characterize pore networks in structural materials. The VDF improves upon existing pore-related metrics reported in the literature by simultaneously accounting for pore clustering, pore sizes, and pore locations relative to free surface, all of which have been shown to influence mechanical behavior of porous materials. To isolate the effect of pore structure on fracture behavior and to assess the performance of the VDF relative to other pore-related metrics, numerical fracture simulations were performed on 120 tensile specimens having statistically similar and explicitly modeled pore instantiations. Prior to simulated loading, the VDF and other common pore-related metrics were recorded for each specimen. Following simulated loading to failure, mechanical properties were recorded for each model, including elastic modulus, yield strength, ultimate tensile strength, percent elongation, and toughness modulus. Based on results from the numerical simulations and subsequent analysis, the following conclusions are drawn:

1. The VDF global maximum exhibits stronger correlations with post-yielding mechanical properties (viz., ultimate tensile strength, elongation, and toughness modulus) than do any of the following pore metrics: fraction porosity, total number of pores, average or maximum reduction of cross-sectional area, average nearest-neighbor distance among pores, and average or maximum pore diameter.
2. The predictive capability of the VDF is illustrated through linear regression. The VDF regression models outperform fraction-porosity regression models in terms of predicting post-yield mechanical properties.
3. The location of global VDF maximum accurately predicts the nominal location of fracture (within $\pm$ 0.2 mm) with 76% frequency and serves as a better indicator of fracture location than the location of the maximum reduced cross-section or the location of the largest pore.
4. Ambiguity scores are introduced to assess the certainty, as a function of error tolerance, of predicting fracture location based on location of the global VDF maximum. Samples with an ambiguity score of 0.7 or less have locations of VDF maximum that correlate strongly with fracture location, as evidenced by a Pearson correlation coefficient of 0.969 and R^2 values between 0.937 and 0.966 from linear regression.
5. The VDF provides a promising metric for predicting variability of mechanical properties due to inhomogeneous pore structures in elastic-plastic materials.

Acknowledgements The authors wish to thank Drs. Jonathan Madison, Bradley Jared, and Brad Boyce for sharing the experimental data used to inform the numerical models in this work. Dr. Branden Kappes is gratefully acknowledged for fruitful discussions that influenced aspects of this work. This research is supported by the National Science Foundation under Grant No. CMMI-1752400 and by the Department of Defense Office of Economic Adjustment (ST1605-19-03). Numerical simulations were performed using resources provided by the University of Utah Center for High Performance Computing.

Appendix

See Tables 5 and 6.

Table 5 Sensitivity of predictions to VDF parameters. The 120 samples described in Sect. 2 were randomly divided into three data sets of 40 samples each. The VDF scaling parameters α and ρ were optimized for each data set and used to blindly predict the fracture location for the remaining 80 samples not included in the optimization

	Data set 1	Data set 2	Data set 3
α	0.096	0.247	0.202
ρ	0.594	0.314	0.167
Number of accurately* predicted samples	49/80**	45/80**	50/80**

*$x_{VDF,max}$ was within 0.2 mm (5%) of x_{fract} (actual fracture)
**The remaining 80 samples not used in Bayesian optimization technique (Shahriari et al. 2016)

Table 6 Condensed tabular input of plastic stress–strain curve

Yield stress [MPa]	Plastic strain
800	0
893	0.002
934	0.004
959	0.006
977	0.008
992	0.01
1004	0.012
1015	0.014
1025	0.016
1034	0.018
1042	0.02
1050	0.022
1057	0.024
1061	0.025
1077	0.03
1105	0.04
1129	0.05
1152	0.06
1173	0.07
1193	0.08
1213	0.09
1232	0.1
1251	0.11
1269	0.12
1288	0.13
1306	0.14
1324	0.15
1342	0.16
1359	0.17
1377	0.18
1395	0.19
1413	0.2
1431	0.21
1449	0.22
1467	0.23
1485	0.24
1504	0.25
1522	0.26
1541	0.27
1559	0.28
1578	0.29
1597	0.3

References

Antou G, Montavon G, Hlawka F, Cornet A, Coddet C (2004) Characterizations of the pore-crack network architecture of thermal-sprayed coatings. Characterizations of the pore-crack network architecture of thermal-sprayed coatings. Mater Charact 53(5):361–372. https://doi.org/10.1016/j.matchar.2004.08.015

ASTM Standard E8/E8M-13a (2013) Standard test methods for tension testing of metallic materials. Tech Rep https://doi.org/10.1520/E0008_E0008M-13A

Bellera CA, Hanley JA (2007) A method is presented to plan the required sample size when estimating regression-based reference limits. J Clin Epidemiol 60(6):610–615. https://doi.org/10.1016/j.jclinepi.2006.09.004

Boyce BL, Salzbrenner BC, Rodelas JM, Swiler LP, Madison JD, Jared BH, Shen YL (2017) Extreme-value statistics reveal rare failure-critical defects in additive manufacturing. Adv Eng Mater 19(8):1700102

Cao TS, Mazière M, Danas K, Besson J (2015) A model for ductile damage prediction at low stress triaxialities incorporating void shape change and void rotation. Int J Solids Struct 63:240–263. https://doi.org/10.1016/j.ijsolstr.2015.03.003

Chawla N, Deng X (2005) Microstructure and mechanical behavior of porous sintered steels. Mater Sci Eng A 390(1):98–112. https://doi.org/10.1016/j.msea.2004.08.046

Chen X, Wu S, Zhou J (2013) Influence of porosity on compressive and tensile strength of cement mortar. Construct Build Mater. https://doi.org/10.1016/j.conbuildmat.2012.11.072

Eichhubl P (2003) Aydin A (2003) Microcrack nucleation, growth, coalescence and propagation in the fatigue failure of a powder metallurgy steel. J Struct Geol 25(1):121–134. https://doi.org/10.1016/S0191-8141(02)00055-X

Fan J, McDowell DL, Horstemeyer MF, Gall K (2003) Cyclic plasticity at pores and inclusions in cast Al'Si alloys. Eng Fract Mech 70(10):1281–1302. https://doi.org/10.1016/S0013-7944(02)00097-8

Fritzen F, Forest S, Böhlke T, Kondo D, Kanit T (2012) Computational homogenization of elasto-plastic porous metals. Int J Plast 29(1):102–119. https://doi.org/10.1016/j.ijplas.2011.08.005

Gunasegaram DR, Farnsworth DJ, Nguyen TT (2009) Identification of critical factors affecting shrinkage porosity in permanent mold casting using numerical simulations based on design of experiments. J Mater Process Technol. https://doi.org/10.1016/j.jmatprotec.2008.03.044

Gurson AL (1977) Continuum theory of ductile rupture by void nucleation and growth: part 1 - yield criteria and flow rules for porous ductile media. J Eng Mater Technol Trans ASME. https://doi.org/10.1115/1.3443401

Hogan JD, Farbaniec L, Sano T, Shaeffer M, Ramesh K (2016) The effects of defects on the uniaxial compressive strength and failure of an advanced ceramic. Acta Materialia 102:263–272. https://doi.org/10.1016/j.actamat.2015.09.028

Hogg R, McKean J, Craig A (2012) Introduction to Mathematical Statistics. Pearson Education. https://books.google.com/books?id=YdwsAAAAQBAJ

Huang T, Gong Y (2018) A multiscale analysis for predicting the elastic properties of 3D woven composites containing void defects. Compos Struct 185:401–410. https://doi.org/10.1016/j.compstruct.2017.11.046

Hyun S, Murakami K, Nakajima H (2001) Anisotropic mechanical properties of porous copper fabricated by unidirectional solidification. Mater Sci Eng A 299(1):241–248. https://doi.org/10.1016/S0921-5093(00)01402-7

Jahed Armaghani D, Tonnizam Mohamad E, Momeni E, Narayanasamy MS, Mohd Amin MF (2015) An adaptive neuro-fuzzy inference system for predicting unconfined compressive strength and Young's modulus: a study on Main Range granite. Bull Eng Geol Environ 74(4):1301–1319. https://doi.org/10.1007/s10064-014-0687-4

Kabatova M, Dudrova E, WRONSKI AS (2009) Microcrack nucleation, growth, coalescence and propagation in the fatigue failure of a powder metallurgy steel. Fatigue Fract Eng Mater Struct 32(3):214–222. https://doi.org/10.1111/j.1460-2695.2009.01328.x

Khademi F, Jamal SM, Deshpande N, Londhe S (2016) Predicting strength of recycled aggregate concrete using Artificial Neural Network, Adaptive Neuro-Fuzzy Inference System and Multiple Linear Regression. Int J Sustain Built Environ 5(2):355–369. https://doi.org/10.1016/j.ijsbe.2016.09.003

Khdir YK, Kanit T, Zaïri F, Naït-Abdelaziz M (2015) A computational homogenization of random porous media: effect of void shape and void content on the overall yield surface. Eur J Mech A 49:137–145. https://doi.org/10.1016/j.euromechsol.2014.07.001

Kramer SLB, Ivanoff TA, Madison JD, Lentfer AP (2019) Evolution of damage and failure in an additively manufactured 316L SS structure: experimental reinvestigation of the third Sandia fracture challenge. Int J Fract 218(1–2):63–84. https://doi.org/10.1007/s10704-019-00357-x

Kramer SL, Jones A, Mostafa A, Ravaji B, Tancogne-Dejean T, Roth CC, Bandpay MG, Pack K, Foster JT, Behzadinasab M et al (2019) The third Sandia Fracture Challenge: predictions of ductile fracture in additively manufactured metal. Int J Fract 218(1–2):5–61

Levine BG, Stone JE, Kohlmeyer A (2011) Fast analysis of molecular dynamics trajectories with graphics processing units'Radial distribution function histogramming. J Comput Phys 230(9):3556–3569. https://doi.org/10.1016/j.jcp.2011.01.048

Li Z, Jing Y, Guo H, Sun X, Yu K, Yu A, Jiang X, Yang XJ (2019) Study of 3D pores and its relationship with crack initiation factors of aluminum alloy die castings. Metallurg Mater Trans B 50(3):1204–1212. https://doi.org/10.1007/s11663-019-01550-y

Lyubartsev AP, Laaksonen A (1995) Calculation of effective interaction potentials from radial distribution functions: a reverse Monte Carlo approach. Phys Rev E 52:3730–3737. https://doi.org/10.1103/PhysRevE.52.3730

Madison JD, Underwood OD, Swiler LP, Boyce BL, Jared BH, Rodelas JM, Salzbrenner BC (2018) In: AIP Conference Proceedings. https://doi.org/10.1063/1.5031506

Masmoudi M, Kaddouri W, Kanit T, Madani S, Ramtani S, Imad A (2017) Modeling of the effect of the void shape on effective ultimate tensile strength of porous materials: numerical homogenization versus experimental results. Int J Mech Sci 130:497–507. https://doi.org/10.1016/j.ijmecsci.2017.06.011

Orsini V, Zikry M (2001) Void growth and interaction in crystalline materials. Int J Plast 17(10):1393–1417. https://doi.org/10.1016/S0749-6419(00)00091-7

Rao S, Cunningham R, Ozturk T, Rollett AD (2016) Measurement and analysis of porosity in Al-10Si-1Mg components additively manufactured by selective laser melting. Mater Perform Charact 5(5):20160037. https://doi.org/10.1520/MPC20160037

Shahriari B, Swersky K, Wang Z, Adams RP, de Freitas N (2016) Taking the human out of the loop: a review of Bayesian optimization. Proc IEEE 104(1):148–175. https://doi.org/10.1109/JPROC.2015.2494218

Sholl DS, Lively RP (2015) Defects in metal'organic frameworks: challenge or opportunity? J Phys Chem Lett 6(17):3437–3444. https://doi.org/10.1021/acs.jpclett.5b01135

Slotwinski JA, Garboczi EJ, Hebenstreit KM (2014) Porosity measurements and analysis for metal additive manufacturing process control. J Res Natl Inst Stand Technol 119:494

Smith M (2014) ABAQUS/Standard User's Manual, Version 6.14. Dassault Systèmes Simulia Corp, United States

Spear AD, Czabaj MW, Newell P, DeMille K, Phung BR, Zhao D, Creveling P, Briggs N, Brodbine E, Creveling C et al (2019) The third Sandia Fracture Challenge: from theory to practice in a classroom setting. Int J Fract 218(1–2):171–194

Su X, Yang Z, Liu G (2010) Monte Carlo simulation of complex cohesive fracture in random heterogeneous quasi-brittle materials: a 3D study. Int J Solids Struct 47(17):2336–2345. https://doi.org/10.1016/j.ijsolstr.2010.04.031

Tvergaard V (Elsevier, 1989), pp. 83 – 151. https://doi.org/10.1016/S0065-2156(08)70195-9

Tvergaard V (1981) Influence of voids on shear band instabilities under plane strain conditions. Int J Fract. https://doi.org/10.1007/BF00036191

Varna J, Joffe R, Berglund L, Lundström T (1995) Effect of voids on failure mechanisms in RTM laminates. Composit Sci Technol 53(2):241–249. https://doi.org/10.1016/0266-3538(95)00024-0

Voisin T, Calta NP, Khairallah SA, Forien JB, Balogh L, Cunningham RW, Rollett AD, Wang YM (2018) Defects-dictated tensile properties of selective laser melted Ti-6Al-4V. Mater Des 158:113–126. https://doi.org/10.1016/j.matdes.2018.08.004

von Lilienfeld OA, Ramakrishnan R, Rupp M, Knoll A (2015) Fourier series of atomic radial distribution functions: a molecular fingerprint for machine learning models of quantum chemical properties. Int J Quant Chem 115(16):1084–1093. https://doi.org/10.1002/qua.24912

Watring DS, Carter KC, Crouse D, Raeymaekers B, Spear AD (2019) Mater Sci Eng A. https://doi.org/10.1016/j.msea.2019.06.003